Available online at www.sciencedirect.com
ScienceDirect
International Journal of Heat and Mass Transfer 50 (2007) 1238–1247
International Journal of HEAT and MASS TRANSFER
www.elsevier.com/locate/ijhmt

Chaotic analysis of mixing enhancement in steady laminar flows through multiple pipe bends

A. Yamagishi, T. Inaba *, Y. Yamaguchi

Department of Mechanical Engineering, Osaka University, 2-1 Yamadaoka, Suita, Osaka 565-0871, Japan

Received 17 April 2006; received in revised form 25 August 2006
Available online 4 December 2006

Abstract

Using numerical simulations, properties of the flow and heat transfer in multiple pipe bends composed of 90°-bends are investigated for various switching angles, and the mixing performance is compared by means of various trajectory-based analyses. Although the behavior of both the secondary flow and Nusselt number show a periodic feature, they do not completely correspond with each other. The Lyapunov exponent quantitatively exhibits a distinct difference in the mixing depending on the switching angle, while the Poincaré map depicts a specific aspect even in a long-term. The residence time distribution is a potential indicator reflecting the flow structure with time-information.

Keywords: Multiple pipe bends; Numerical analysis; Chaotic advection; Mixing; Lyapunov exponent

1. Introduction

The motion of particles in a periodic flow may be chaotic even if the velocity field itself is of a rather simple steady laminar flow in case the fluid elements are subjected to iterative stretching and folding. This chaotic advection has been a hot topic of interest for many researchers as a fascinating non-linear phenomena, and has often been characterized by the Poincaré section. Ottino [1] summarized the analysis and modeling of the chaotic mixing of two-dimensional periodic flows and three-dimensional steady flows.

Flow in multiple pipe bends, in which bends are periodically connected with a certain switching angle, is one of the typical examples of the chaotic advection. Curved pipes are widely used in the industrial field, e.g., as heat exchangers and chemical reactors, owing to their high-performance in heat transfer and mixing. However, in regular coiled pipes, the counter-rotating secondary flow vortices divide the cross-sectional flow field into two closed regions, which prevents homogenous mixing. Meanwhile, in multiple pipe bends, the Coriolis force acts on the fluid due to the torsion of the coordinate system when the curvature plane switches, in addition to the centrifugal force due to the curvature [2]. This enhances mixing and heat transfer without additional pressure drops compared to usual coiled pipes, and this enhancement is effectively realized in laminar flows. Taking advantage of the low-shear stress compared to the turbulent mixing, potential applications are also expected in dealing with fragile or heat-sensitive products such as chemical products, biological products, food, and human blood, besides conventional application to such as heat exchangers.

Jones et al. [3] numerically analyzed steady laminar flows in curved pipes composed of 180°-bends and investigated the effect of switching angle on the mixing.

Acharya et al. [4] numerically simulated the mixing and heat transfer using a simplified flow field in various multiple pipe bends with the switching angles of 90°. They experimentally examined the heat transfer in a curved pipe system made of 180°-bends as well, and indicated that the heat transfer was enhanced by 6%–8% compared to

* Corresponding author. Tel.: +81 6 6879 7267; fax: +81 6 6879 7255.
E-mail address: inaba@mech.eng.osaka-u.ac.jp (T. Inaba).

0017-9310/$ - see front matter © 2006 Elsevier Ltd. All rights reserved.
doi:10.1016/j.ijheatmasstransfer.2006.09.033

Nomenclature

a	pipe radius
Dn	Dean number
d	distance between neighboring fluid particles
d_p	modified average pointwise dimension
L	length of the convolute line
m	point number for spatial average
M	number of points for spatial average
n	step number
N	number of steps for temporal average
Nu	Nusselt number
$\overline{Nu}$	peripherally averaged mean Nusselt number
p	pressure
Pr	Prandtl number $= \nu/\alpha$
Q	flow rate
r	radial coordinate
R	radius of curvature of the bend
Re	Reynolds number $= 2aW/\nu$
t	time
T	temperature
T_b	dimensionless temperature
T_{bulk}	bulk temperature
T_{in}	inlet temperature
t_m	mean residence time
T_w	wall temperature
u	radial velocity
v	azimuthal velocity
V	fluid volume in the multiple pipe bends
w	axial velocity
W	average axial velocity
Greek symbols	
α	thermal diffusivity
δ	radius ratio $(=a/R)$
θ	axial angular coordinate
λ	Lyapunov exponent
$\bar{\lambda}$	average Lyapunov exponent
ν	kinematic viscosity
ρ	density
τ	time that a particle reaches the next axial cell
φ	azimuthal coordinate
Φ	switching angle
ψ	stream function

the coiled pipe for the Reynolds number ranging from 3000 to 10,000. They also compared the mixing and heat transfer in 180°-bends with different switching angles by numerical simulations [5]. They explored the mechanism of the enhancement in heat transfer partly relating with mixing, and concluded that the mixing effect alone is not sufficient to explain the mechanism thoroughly.

Mokrani et al. [6] performed experiments of the flow in multiple pipe bends consisting of 90°-bends with the switching angle of 90° for the Reynolds numbers between 60 and 200 using carboxymethyl cellulose (CMC) solution as the sample fluid, and determined that the heat transfer was enhanced by 14%–28% compared to the coiled pipe. Castelain et al. [7,8] carried out experiments on the distribution of the residence time by means of tracer particles in the same pipe as in [6] and analyzed the mixing performance. For the Reynolds numbers greater than 2500, they obtained more than 20% decrease in axial dispersion for the 33-bend chaotic system compared to a helical one. Furthermore, they extended the experiments to the range of the Reynolds numbers between 30 and 30,000, and investigated the relation between the thermal performance and energy consumption [9].

The present authors have performed simulations on the mixing and heat transfer in various multiple pipe bends with 90° switching angle, and showed the temperature and velocity fields [10]. In this paper, the properties of the flow and heat transfer in multiple pipe bends composed of 90°-bends are investigated for various switching angles, and detailed comparisons of the mixing performance are carried out by means of non-linear chaotic analyses including the Lyapunov exponent, Poincaré map and the residence time distribution.

2. Simulation method

Fig. 1 shows the models of the multiple pipe bends considered in this study. All models are composed of 90°-bends with a constant radius of curvature, and the multiple pipe bends are obtained by periodically connecting each bend with a certain switching angle Φ, e.g., $\Phi = 45°$, 90°, and 180° correspond to Fig. 1(a)–(c), respectively. A coiled pipe without periodic change in the switching angle depicted as Fig. 1(d) is equivalently modeled as $\Phi = 0°$.

A steady laminar flow of an incompressible fluid is assumed in the analysis. The coordinate system of (r, φ, θ) illustrated in Fig. 2 is applied, where the corresponding Cartesian coordinates (x, y, z) is expressed as

$$\begin{cases} x = (R + r\cos\varphi)\cos\theta, \\ y = (R + r\sin\varphi)\sin\theta, \\ z = r\sin\varphi. \end{cases} \tag{1}$$

All variables are non-dimensionalized based on the radius of the pipe a, average axial velocity W, and inlet and wall temperatures T_{in} and T_w, respectively,

$$\begin{aligned} &r^* = \frac{r}{a}, \quad \varphi^* = \varphi, \quad \theta^* = \theta, \quad R^* = \frac{R}{a}, \\ &u^* = \frac{u}{W}, \quad v^* = \frac{v}{W}, \quad w^* = \frac{w}{W}, \quad p^* = \frac{p}{\rho W^2}, \\ &T^* = \frac{T_w - T}{T_w - T_{in}}. \end{aligned} \tag{2}$$

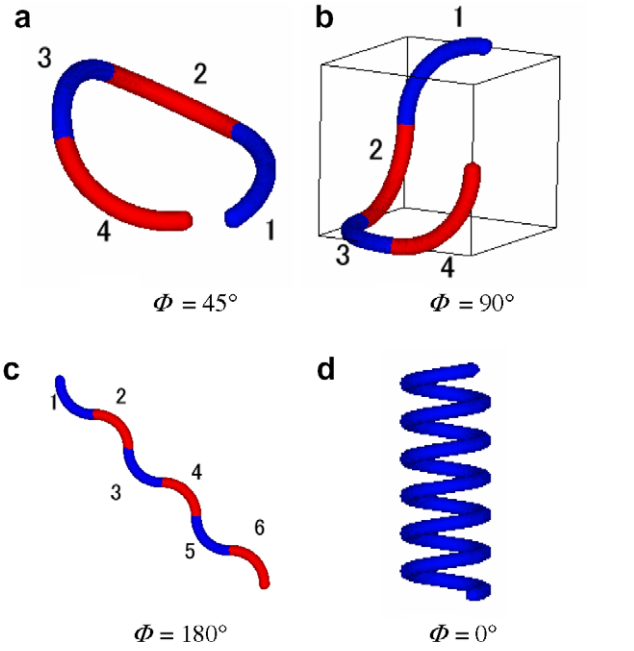

Fig. 1. Multiple pipe bends composed of 90°-bends with various switching angles Φ.

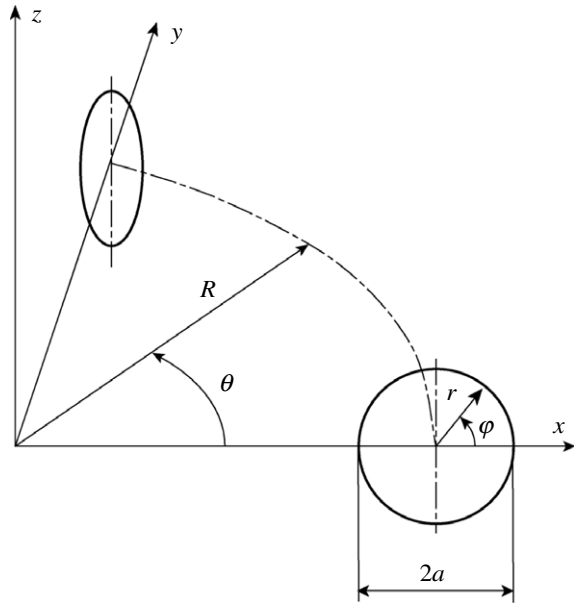

Fig. 2. Coordinate system.

In the following expressions, we omit the asterisks of these dimensionless variables. When the curvature ratio $\delta = a/R$ is small and the Reynolds number is moderate, the transverse velocity components u and v are small in comparison with the axial component w. In such a case, the effect of axial diffusion is negligibly small and the governing equations can be parabolized [11], so that the calculation is carried out using a space marching technique. The equation of continuity, and the parabolized Navier–Stokes equation and energy equation are then expressed as:

$$\frac{\partial}{\partial r}(rhu) + \frac{\partial}{\partial \varphi}(hv) + \frac{\partial}{\partial \theta}(rw) = 0, \tag{3}$$

$$\frac{\partial}{\partial r}(b_r F) + \frac{\partial}{\partial \varphi}(b_\varphi F) + \frac{\partial}{\partial \theta}(b_\theta F) = -P_F + S_F + \frac{R_F}{C_0} + \frac{1}{C_0}\left\{\frac{\partial}{\partial r}\left[c_r \frac{\partial}{\partial r}(Fd)\right] + \frac{\partial}{\partial \varphi}\left[c_\varphi \frac{\partial}{\partial \varphi}(Fd)\right]\right\}, \tag{4}$$

where $h = R + r\cos\varphi$ and the other coefficients are summarized in Table 1. The pressure p can be separated into the sectional mean pressure and transverse component according to Ghia [12].

$$p(r, \varphi, \theta) = \bar{p}(\theta) + p'(r, \varphi). \tag{5}$$

To close the system of equations, the following equation to ensure the constant volume of the flow through the cross-section is considered.

$$\frac{\partial}{\partial \theta}\int_0^{2\pi}\int_0^1 rw\mathrm{d}r\mathrm{d}\varphi = 0. \tag{6}$$

The isothermal Poiseuille flow is assumed at the inlet of the bends with $T_{in} = 1$, and the non-slip boundary condition is applied besides the constant wall temperature of $T_w = 0$ at the wall.

Eq. (4) is discretized for each control volume on the staggered grid, and the convective terms and viscosity terms are approximated by the 3rd-order upwind scheme and second-order central difference scheme, respectively, while the SIMPLE algorithm is adopted to calculate the velocity and pressure. Based on the experience from the previous work [10], the grid spacing of $\Delta r = 1/40$, $\Delta\varphi = 2\pi/96$ and $\Delta\theta = (\pi/2)/3600$ is employed except for the transition parts, where $\Delta\theta$ varies according to the switching angle as explained below.

In our previous work [10], we have investigated the velocity and temperature fields in the multiple pipe bends with the switching angle $\Phi = 90°$ and in the helical coiled pipe. For further analysis, the switching angle Φ is varied from 0 to 180° with a fixed bend angle of 90° in this study.

Table 1
Coefficients of governing equations in Eq. (4)

F	C_0	b_r	b_φ	b_θ	c_r	c_φ	D
u	$\frac{Re}{2}$	rhu	hv	rw	rh	$\frac{h}{r}$	1
v	$\frac{Re}{2}$	r^2hv	rhv	r^2w	r^3h	rh	$\frac{1}{r}$
w	$\frac{Re}{2}$	rh^2u	h^2v	rhw	rh^3	$\frac{h^3}{r}$	$\frac{1}{h}$
T	$\frac{RePr}{2}$	rhu	hv	rw	rh	$\frac{h}{r}$	1

P_F	S_F	R_F
$rh\frac{\partial p'}{\partial r}$	$hv^2 + rw^2\frac{\partial h}{\partial r}$	$-\frac{2h}{r}\frac{\partial v}{\partial \varphi} - \frac{hu}{r} - \frac{1}{r}\frac{\partial h}{\partial \varphi}v - \frac{r}{h}\frac{\partial h}{\partial r}\left(2\frac{\partial w}{\partial \theta} + u\frac{\partial h}{\partial r} + \frac{v}{r}\frac{\partial h}{\partial \varphi}\right)$
$rh\frac{\partial p'}{\partial \varphi}$	$rw^2\frac{\partial h}{\partial \varphi}$	$2h\frac{\partial u}{\partial \varphi} + \frac{\partial h}{\partial \varphi}u + r\frac{\partial h}{\partial r}v - \frac{r}{h}\frac{\partial h}{\partial \varphi}\left(2\frac{\partial w}{\partial \theta} + u\frac{\partial h}{\partial r} + \frac{v}{r}\frac{\partial h}{\partial \varphi}\right)$
$rh\frac{\partial \bar{p}}{\partial \theta}$	0	$r\frac{\partial h}{\partial r}\frac{\partial u}{\partial \theta} + \frac{\partial h}{\partial \varphi}\frac{\partial v}{\partial \theta}$
0	0	0

A short sub-segment, in which the switching angle is sequentially changed, is inserted at each connecting section as a transition part in order to avoid the unfavorable discontinuity in the pressure gradient due to the abrupt change in the direction of the centrifugal force. The sub-segment consists of short pipe-elements connected with each other with a local switching angle of 7.5°, and the length and number of pipe-elements are configured so that the total length of the sub-segment is fixed at $\theta = 3.6°$ in the axial direction independent of the switching angle Φ, e.g., 12 pipe-elements with a length of $\theta = 0.3°$ are inserted for $\Phi = 90°$ (=12 × 7.5°).

The simulations are performed for the Dean number ranging from 50 to 400, where the Dean number Dn is defined using the Reynolds number and the radius ratio $\delta = a/R$ as in Eq. (7).

$$Dn = Re\sqrt{\delta}, \tag{7}$$

where δ is fixed at 1/20 in this study.

Prandtl number of the fluid is basically set to 15.8 assuming ethyl-alcohol as the sample fluid while air and water with $Pr = 0.7$ and 7.0, respectively, are also considered for the comparison.

3. Analysis on the secondary flow and heat transfer

Fig. 3 shows the secondary flow patterns for various switching angles at $Dn = 150$ in the ninth bend, where the effect of the inlet boundary condition has almost disappeared and the flow pattern can be considered to be quasi-periodic. Here, the stream function is given by Eq. (8).

$$u = -\frac{1}{rh}\frac{\partial\psi}{\partial\varphi}, \quad v = \frac{1}{h}\frac{\partial\psi}{\partial r}. \tag{8}$$

When the curvature plane switches at the bend connection, the Dean roll-cells move in the cross-section and the Coriolis force acts perpendicularly to the direction of the secondary flow velocity vectors in the transition part causing an asymmetric secondary flow pattern (Fig. 3(i)). As advancing further, it approaches to a symmetric one due to the dominance of the centrifugal force. Then, it becomes asymmetric again in latter part of the bend due to the inertia in the movement of the secondary flow field (Fig. 3(iii)). This feature is periodically observed, and stronger secondary flow is basically formed as the switching angle becomes larger except in the case of $\Phi = 180°$, in which the secondary flow pattern is rather distributed especially after the connection due to the complete flip of the curvature (Fig. 3(d)).

Fig. 4 shows the contour of the temperature distribution in the 9th bend for $Pr = 15.8$ and $Dn = 150$, where the dimensionless temperature T_b given by Eqs. (9) and (10) is applied.

$$T_b = \frac{T_w - T}{T_w - T_{bulk}}, \tag{9}$$

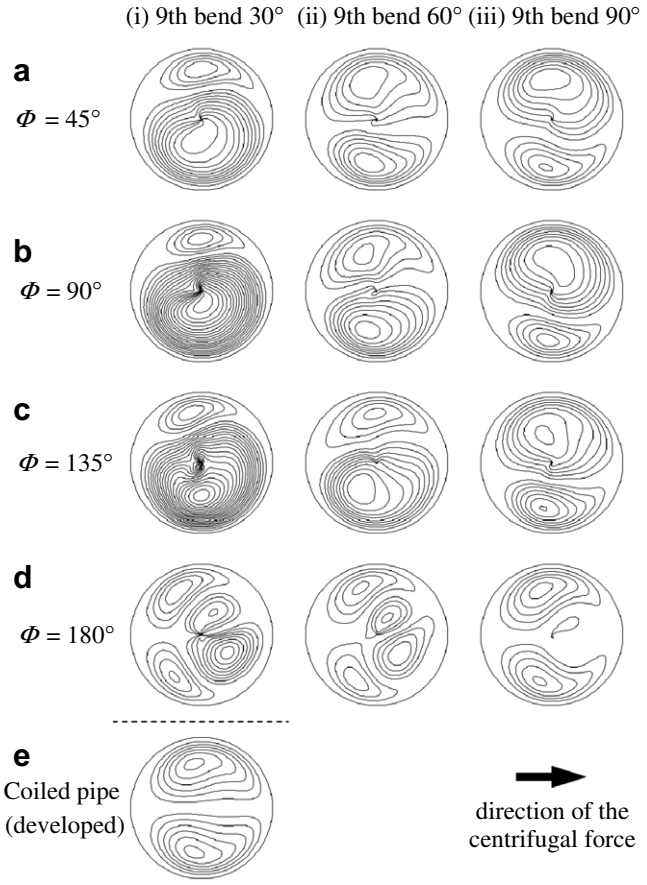

Fig. 3. Secondary flow patterns in the 9th bend ($Dn = 150$). Note that the pattern for $\Phi = 180°$ (d) is not symmetric because a short transition part is inserted between the 90°-bends when switching the curvature plane.

$$T_{bulk} = \frac{1}{\pi}\int_0^{2\pi}\int_0^1 Twr\mathrm{d}r\mathrm{d}\varphi. \tag{10}$$

The temperature distribution in the coiled pipe for high-Prandtl number is similar to the secondary flow pattern, i.e., hot sections are symmetrically separated into two parts. In the multiple pipe bends, on the other hand, the hot section moves corresponding to the alternative change in the relative size of the twin secondary vortices, and thus, the temperature distribution shows a rather complicated feature. For $\Phi = 90°$ and 135°, high-temperature parts come together and spread extensively in the cross-section (Fig. 4(c-iii)), and therefore, the thermal boundary layer at the wall is especially thin compared to the other switching angles.

Fig. 5 shows the axial profile of the cross-sectional average of the mean stream function which represents the strength of the secondary flow, and the peripherally averaged Nusselt number at $Pr = 15.8$ and $Dn = 150$ for various switching angles and for the coiled pipe. The peripherally averaged Nusselt number here is defined as in Eq. (11) using the bulk temperature T_{bulk} and the average of the temperature gradient at the wall in Eqs. (10) and (12), respectively.

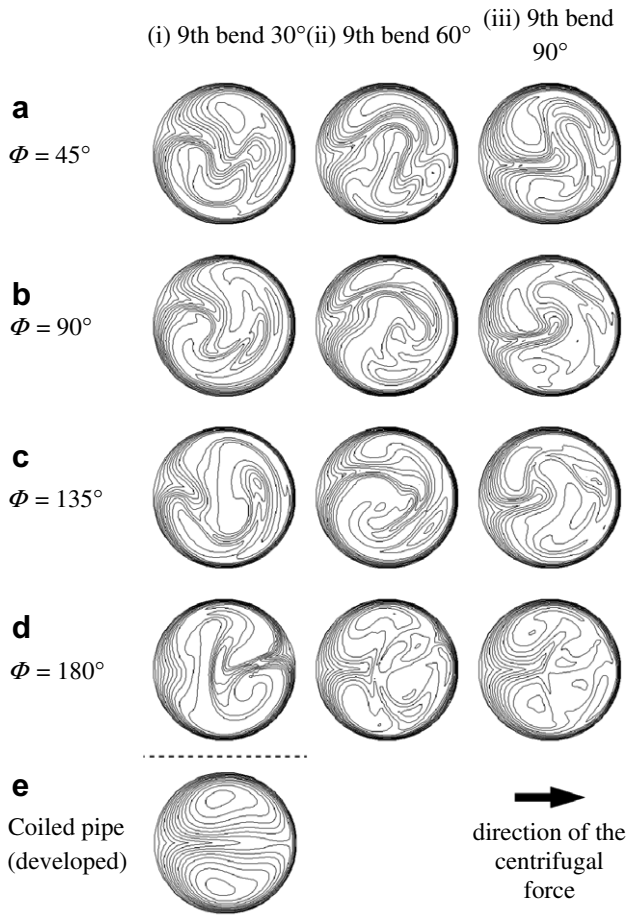

Fig. 4. Temperature distributions in the 9th bend ($Pr = 15.8$, $Dn = 150$).

$$\overline{Nu} = \frac{2}{T_{\text{bulk}}}\left\langle \frac{\partial T}{\partial r} \right\rangle_{r=1}, \tag{11}$$

$$\left\langle \frac{\partial T}{\partial r} \right\rangle_{r=1} = \frac{1}{2\pi}\int_0^{2\pi} \left(\frac{\partial T}{\partial r}\right)_{r=1} r\mathrm{d}\varphi. \tag{12}$$

The strength of the secondary flow in the coiled pipe asymptotically reaches to a constant value while those for multiple pipe bends converge to a quasi-periodic change around after the third bend except for $\Phi = 180°$ in which the secondary flow pattern is multiply-scattered as seen in Fig. 3(d). The amplitude of the fluctuation is the largest for $\Phi = 90°$ at this Dean number. Similar to the stream function, the mean Nusselt number in multiple pipe bends shows a periodic feature although there exists a distinct phase lag to the stream functions depending on the switching angle, and the resulting heat transfer is the highest for $\Phi = 135°$ in contrast to the intensity of the stream function. In addition, the mean Nusselt number for multiple pipe bends is higher than that for the coiled pipe at this high-Prandtl number. However, this advantage over the coiled pipe is not observed at a lower Prandtl number of 0.7.

4. Analysis on the mixing performance

As seen in the previous section, the motion of twin vortices in the transverse section seems to enhance the convective heat transfer through mixing. However, it is difficult to evaluate and compare the mixing performance in complex three-dimensional flows in these multiple pipe bends. In this section, various approaches mostly related to trajectory-based non-linear analyses are examined in order to estimate the mixing performance.

Assuming a tracer fluid particle located at (r_n, φ_n) in the nth plane in θ-direction, the subsequent position in the $(n+1)$th plane (r_{n+1}, φ_{n+1}) is denoted as:

$$\begin{aligned} r_{n+1} &= r_n + \mathrm{d}r \\ \varphi_{n+1} &= \varphi_n + \mathrm{d}\varphi \end{aligned} \tag{13}$$

Considering the following relations in Eqs. (14) and (15), (r_{n+1}, φ_{n+1}) is determined as in Eq. (16), and the trajectory of a particle is thus calculated iteratively.

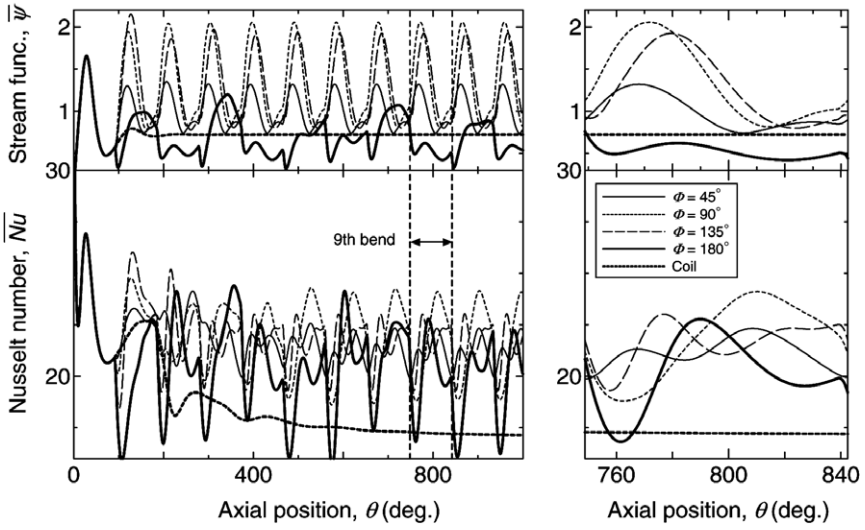

Fig. 5. Variations of stream function $\bar{\psi}$ and mean Nusselt number ($Pr = 15.8$, $Dn = 150$). Enlarged feature at the 9th bend is shown in the right which corresponds to the region where the secondary flow patterns and temperature distributions are shown in Figs. 3 and 4.

$$\frac{dr}{dt} = u, \quad \frac{d\varphi}{dt} = \frac{1}{r}v, \quad \frac{d\theta}{dt} = \frac{1}{h}w \tag{14}$$

$$\frac{dr}{d\theta} = h\frac{u}{w}, \quad \frac{d\varphi}{d\theta} = \frac{h}{r}\frac{v}{w} \tag{15}$$

$$r_{n+1} = r_n + \frac{hu}{w}d\theta$$
$$\varphi_{n+1} = \varphi_n + \frac{hv}{rw}d\theta \tag{16}$$

In this section, all of the tracer trajectory points are initially located at the end of the 40th bend where the flow is considered to be fully developed.

4.1. Line-stretching

Regarding the chaotic advection, the mixing performance can be evaluated as the evolution of the distance between two nearby tracers that expands through the stretching, cutting, and stacking of the flow denoted as "baker's transformation" in [13]. In order to visualize and evaluate this baker's transformation, tracer trajectory points are initially aligned densely on the line vertical to the centrifugal force, and the transversal intersection of the trajectories are examined here. Fig. 6 shows the intersection of the trajectories for $Dn = 150$ at the end of 3rd and 6th bends, where as many as 20,000 points are adopted so that the sequence of the points can be seen as a stretched line even after advancing further to the axial direction. The points form regular convoluted lines in the coiled pipe (Fig. 6(e) and (j)) and this structure is similar to the secondary flow pattern shown in Fig. 3(e) with twin concentric circles, whereas the points spread out over the intersection in other multiple pipe bends in Fig. 6(a)–(d) and (f)–(i), showing the chaotic mixing inside. The line seems to be more stretched as the switching angle becomes larger until $\Phi = 135°$ (Fig. 6(a)–(d)), and some parts are not apparently recognized as line after 6 bends for $\Phi = 90°$ and 135° despite the huge number of tracer points (Fig. 6(g) and (h)). Distinctly divided three regions can be observed in Fig. 6(i) for $\Phi = 180°$ indicating a rather localized mixing in this case.

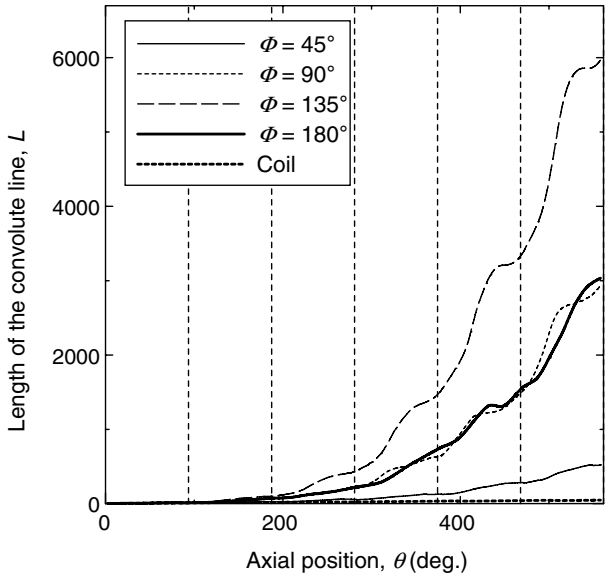

Fig. 7. Evolution of the length of the convolute line as the sum of the distance between neighboring points in Fig. 6 ($Dn = 150$).

The evolution of the line length L calculated as the sum of the distance between neighboring points is depicted in Fig. 7 as a quantitative measure. The line length L exponentially increases with a periodic feature as advancing to the axial direction, and the increase is the largest for $\Phi = 135°$. The line-lengths for $\Phi = 90°$ and 180° are comparable at this Dean number although the stretching fea-

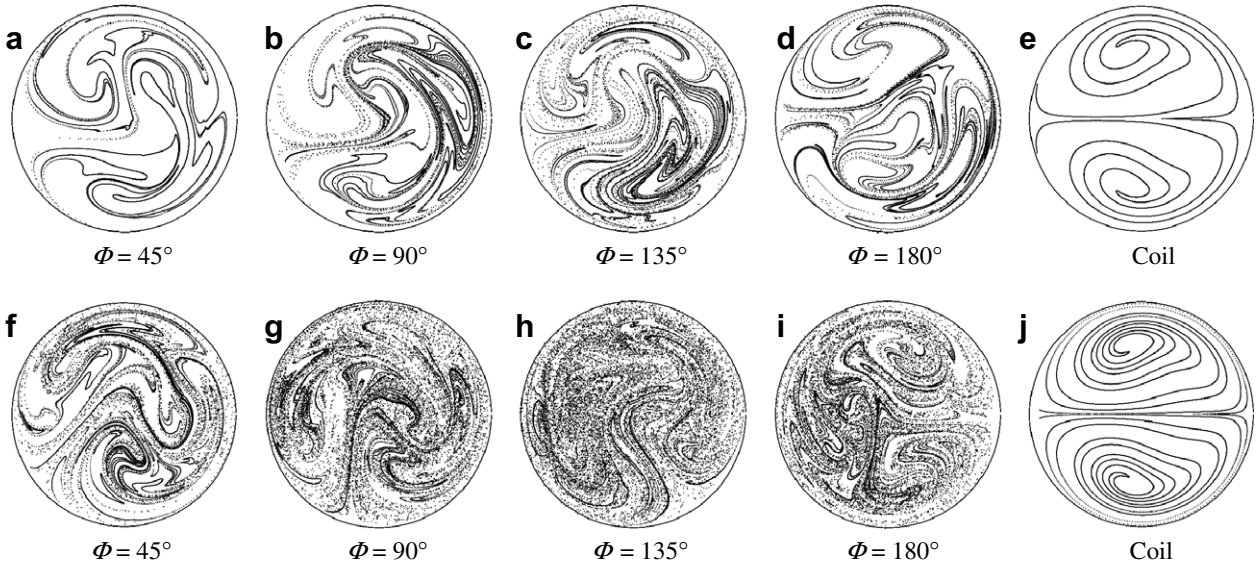

Fig. 6. Intersections of the trajectories of 20,000 points initially aligned on the line perpendicular to the centrifugal force for $Dn = 150$ at the end of the 3rd bend (a)–(e), and the 6th bend (f)–(j); (e) and (j), respectively are for the coiled pipe at the corresponding axial locations.

ture seems rather different. It is also clear that the line-stretching does not necessarily correspond to the intensity of the secondary flow shown as the stream function in Fig. 5, in which the amplitude increases as the switching angle Φ becomes larger until $\Phi = 90°$ and drastically decrease for $\Phi = 180°$.

4.2. Lyapunov exponent

The line stretching shown above is a technique to quantitatively evaluate the line length by densely allocating the trajectory points on line, and the length evolves exponentially as advancing in the axial direction. This exponential increase is handled more in general here. When the distance between two nearby trajectories at a certain time t evolves exponentially to the time, i.e., when the distance is expressed as an exponential function of the time delay τ as:

$$d(t+\tau) = d(t)\exp(\lambda\tau), \tag{17}$$

this value λ is denoted as Lyapunov exponent and takes a positive value in a chaotic system. The Lyapunov exponent in a long-term average for a system with an infinite space is often given by

$$\lambda = \lim_{\tau\to\infty} \frac{1}{\tau} \log\left(\frac{d(t+\tau)}{d(t)}\right). \tag{18}$$

However, this definition is apparently not valid for a finite system like in multiple pipe bends where the distance $d(t+\tau)$ in the transversal intersection may not diverge to infinite even for $\tau \to \infty$. Therefore, we adopted the localized Lyapunov exponent [14] defined as the temporal average of short-term Lyapunov exponents $\lambda_n (n = 1 \sim N)$ with a time delay Δt expressed as in Eq. (19).

$$\overline{\lambda_N} = \frac{1}{N}\sum_{k=1}^{N} \lambda_n, \quad \lambda_n = \frac{1}{\Delta t}\log\left(\frac{\overline{d_n}}{d_0}\right),$$
$$\overline{d_n} = \frac{1}{M}\sum_{m=1}^{M} d_m|_{t=t_n+\Delta t}, \tag{19}$$

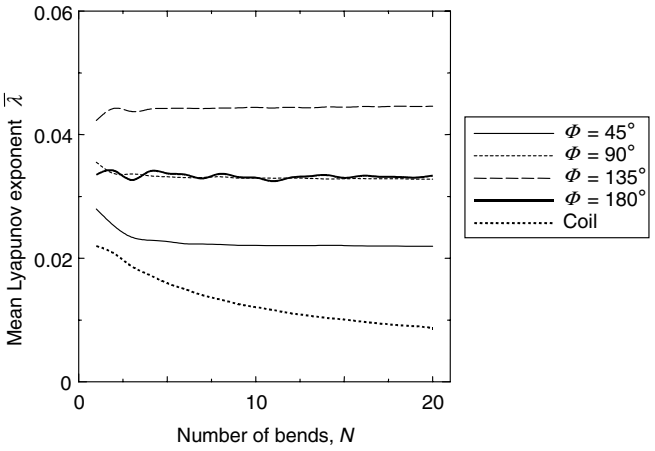

Fig. 9. Evolution of the mean Lyapunov exponents ($Dn = 150$).

where $\overline{d_n}$ is the spatial average of the distance d_m ($m = 1 - M$) from the noticed point to the surrounding partner trajectories at step $n+1$ that are located on a circle with a radius of d_0 at step n, i.e., M partner trajectories are re-selected around the noticed point so that the distance is always reset to d_0 at each step. In this manner, the calculation of the Lyapunov exponent in a finite system is enabled at each point in the intersection. The number of partner trajectories M and the initial distance d_0 for the spatial average are set to 100 and 1.0×10^{-5}, respectively.

Fig. 8 shows the distributions of the localized Lyapunov exponent for $Dn = 150$, where the temporal average is calculated until the end of the 1st and the 20th bends. The complexity of the distribution for the short-term average illustrated in Fig. 8(a)–(e) is similar to the line structures in Fig. 6, i.e., the distribution gets more anfractuous as the switching angle becomes larger until $\Phi = 135°$, and it becomes less complicated for the $\Phi = 180°$ whereas it shows a symmetric feature for the coiled pipe. The distributions are almost uniform at the end of the 20th bend and no clear structure can be seen except for the coiled pipe (Fig. 8(f)–(j)).

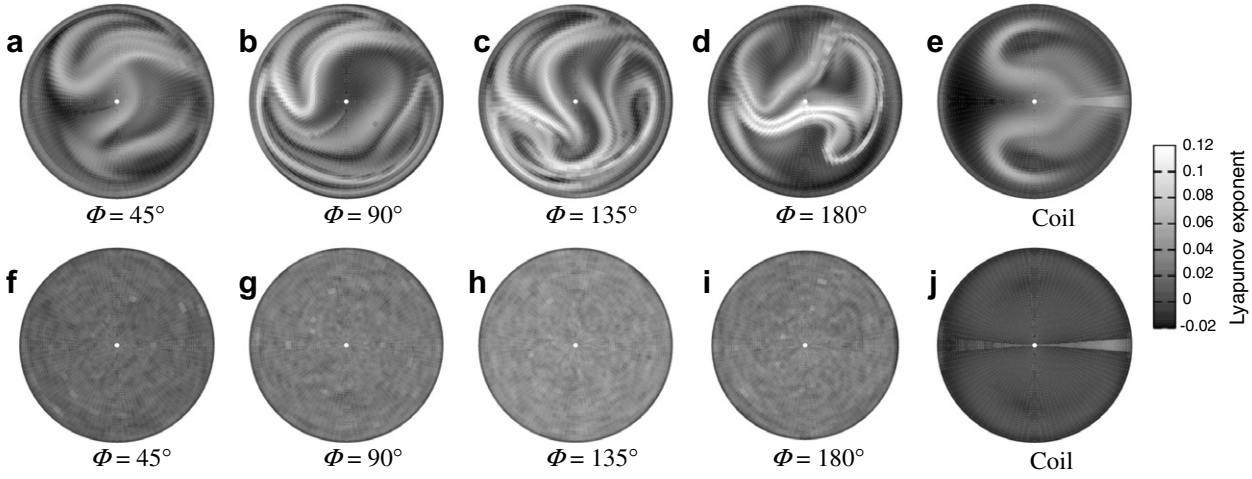

Fig. 8. Distributions of the localized Lyapunov exponent calculated until the end of the1st bend (a)–(e), and the 20th bend (f)–(j). ($Dn = 150$).

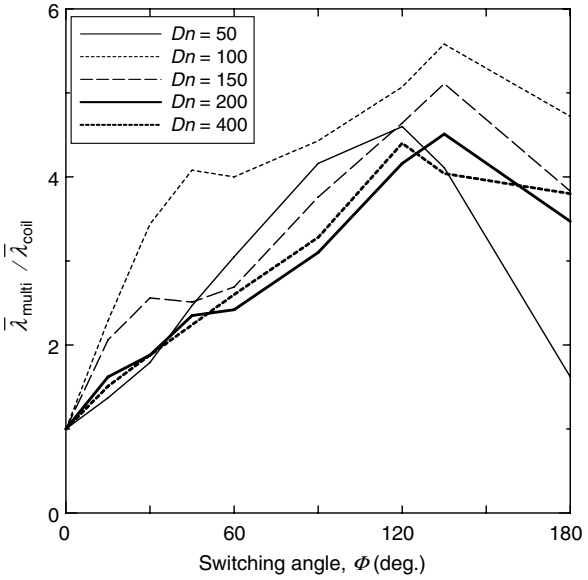

Fig. 10. Dependence of the mean Lyapunov exponents on the switching angle for various Dean numbers. The values at the 20th bend are adopted as the ratio to those for coiled pipe for comparison.

Fig. 9 shows the evolution of the mean Lyapunov exponent averaged over the whole intersection as a quantitative measure. The mean Lyapunov exponent is again the highest for $\Phi = 135°$ and it takes similar value for $\Phi = 90°$ and 180° as well as the line-stretching shown in Fig. 7. The Lyapunov exponent converges to a certain value as advancing in the axial direction except for the coiled pipe.

The dependence of mean Lyapunov exponents on the switching angle for various Dean numbers are summarized in Fig. 10, where the values at the 20th bend are depicted as the ratio to those for coiled pipe for comparison. For a low-Dean number of $Dn = 50$, the peak position of the Lyapunov exponent lies around the switching angle $\Phi = 120°$ and the Lyapunov exponent drastically decreases at $\Phi = 180°$. Meanwhile, this peak position shifts to a larger switching angle around $\Phi = 135°$, and the relative decrease for $\Phi = 180°$ becomes small for higher Dean numbers.

4.3. Poincaré map

Poincaré map is often used to visualize the flow structure by superimposing the intersections of several trajectories on a single plane, and is considered to be a practical method in order to evaluate the mixing performance. Fig. 11 shows the Poincaré maps for various switching angles Φ at $Dn = 50$ and 150. Eighteen points are initially located on the center line perpendicular to the direction of centrifugal force, and the intersection of these trajectories at the end of each bend is superimposed on a same plane until 500th bend in these maps here. A distinct structure in the contrast means that the motion of particles is trapped in the high-density region and restricted there, and therefore, a less-structured map, in which the particles may freely move over the pipe cross-section, is preferred regarding the better mixing. In explaining the chaotic advection, the well-structured region with high-density points and the less-structured region with well-scattered points are often called "regular region" and "chaotic region," respectively beside the region with sparse points illustrated as brighter shade denoted as 'island.' At a low-Dean number of $Dn = 50$, the twin islands seen for $\Phi = 15°$ (Fig. 11(a1)) gradually becomes smaller as Φ gets larger (Fig. 11(a2) and (a3)), and no regular region or island can be observed for $\Phi = 135°$ (Fig. 11(a4)). Very characteristic structure with eight isolated regular regions appears for $\Phi = 180°$, resulting in a significant drop in the mixing performance as shown for the Lyapunov exponent in Fig. 10. At a high-Dean number of $Dn = 150$, on

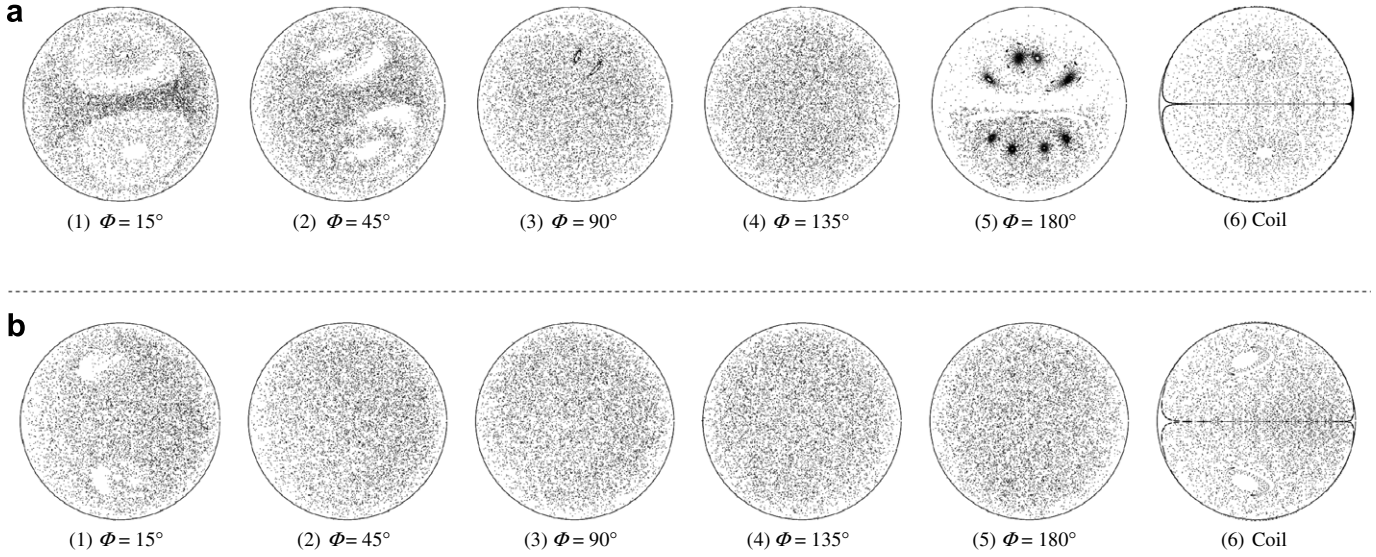

Fig. 11. Poincaré maps for various switching angles Φ at (a) $Dn = 50$, and (b) $Dn = 150$.

Table 2
Fractal dimensions of Poincaré map

Φ	$Dn = 50$	150
45°	1.72	1.67
90°	1.74	1.71
135°	1.73	1.73
180°	1.72	1.69
Coil	1.00	1.05

the other hand, the vague islands seen for $\Phi = 15°$ (Fig. 11(b1)) already disappear for $\Phi \geqslant 45°$ (Fig. 11(b1–b5)), and chaotic region spreads over the whole cross-section even for $\Phi = 180°$. As far as the apparent feature of the Poincaré map is concerned, all maps for the switching angles $45° \leqslant \Phi \leqslant 180°$ are quite similar despite the remarkable difference in the Lyapunov exponents in Fig. 9. For the coiled pipe, meanwhile, two distinct islands can be observed for both Dean numbers, and many points are trapped on the periphery and center line to form a regular region (Fig. 11(a6) and (b6)).

In order to quantitatively examine the complexity of the Poincaré map, the fractal dimension is calculated as the pointwise dimension of the point group [15]. The fractal dimensions for various switching angles at Dean numbers $Dn = 50$ and 150 are summarized in Table 2. The fractal dimension takes similar value around 1.7 for $45° \leqslant \Phi \leqslant 180°$, and the differences between them are rather small, whereas it is nearly 1 for the coiled pipe at both Dean numbers, showing that the motion of the fluid particle is not chaotic. Despite the apparent difference in the Poincaré map at $Dn = 50$, its fractal dimension does not seem to be a good quantitative measure in this case; however, the map provides the specific feature even with a long-term superposition until 500th bend, especially for multiple pipe bends with low-mixing performance.

4.4. Residence time distribution

All the analyses shown above are based on the intersection of the trajectories in the pipe, and the information of the time-difference among the trajectories is ignored. The residence-time distribution (RTD) is investigated in order to examine the longitudinal dispersion of fluid particles in the pipe here. The residence time of a trajectory is simply obtained as the time taken to arrive at certain outlet position, and the RTD is obtained with the trajectories of 31 396 points homogeneously allocated at the fully-developed inlet, i.e., at the end of the 40th bend as in the other trajectory-based analyses.

Fig. 12 shows the spatial distributions and histograms of the residence time within 20 bends for various switching

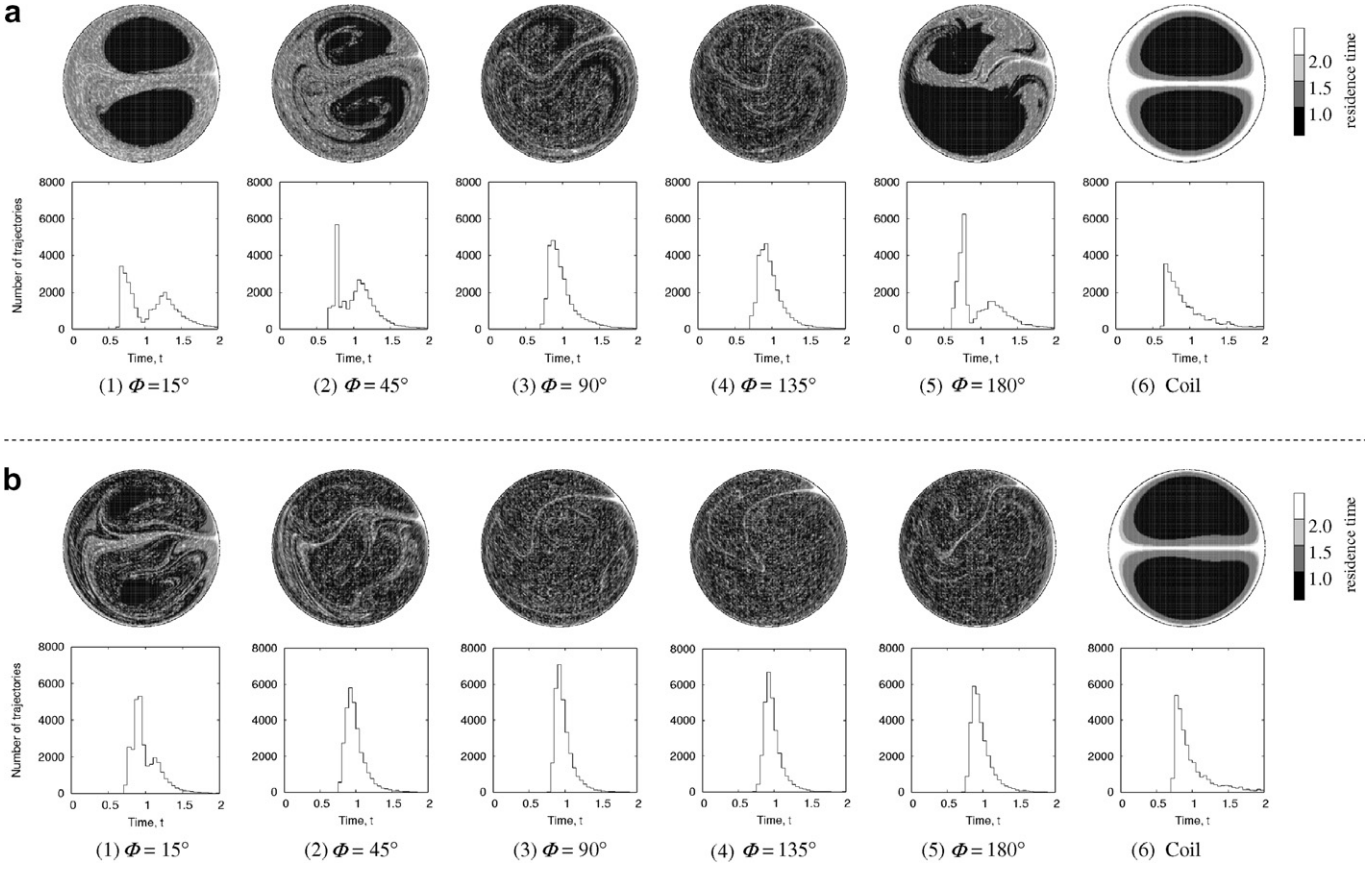

Fig. 12. Spatial distributions (upper) and histograms (lower) of the residence time within 20 bends for various switching angles Φ at (a) $Dn = 50$, and (b) $Dn = 150$.

angles Φ at $Dn = 50$ and 150 as a function of the time normalized by the mean residence-time $t_m = V/Q$, where V and Q denote the volume of the multiple pipe bends and flow rate, respectively. Brighter shade in the spatial distribution denotes longer residence time. At a low-Dean number of $Dn = 50$, twin dark regions are isolated in the spatial distribution and that feature appears as the clear two-peak structure in the histogram for $\Phi = 15°$ (Fig. 12(a1)). The dark regions are more diffused as Φ becomes larger (Fig. 12(a2)–(a4)), and the separated peaks in the histogram come together indicating a homogeneous mixing until $\Phi = 135°$. A large dark region then appears for $\Phi = 180°$ again with two distinct peaks in the histogram. The spatial distribution for the coiled pipe has a symmetric structure with a clear contrast although the histogram has a single peak (Fig. 12(a6)). At a high-Dean number $Dn = 150$, the dark regions may easily be scattered even with a smaller switching angle (Fig. 12(b1)) and is not appreciably different also for $\Phi = 180°$ (Fig. 12(b5)).

5. Concluding remarks

The properties of the flow and heat transfer in multiple pipe bends were investigated for various switching angles with a fixed bend angle of 90° by using numerical simulations, and various comparisons of the mixing performance were carried out by means of trajectory-based analyses.

Both the secondary flow and mean Nusselt number in the fully-developed region resulted in a periodic feature although the intensity of the secondary flow did not necessarily correspond to the mean Nusselt number.

The comparison via the line-stretching and Lyapunov exponent quantitatively showed a distinct difference in the mixing performance while the Poincaré map apparently depicted a specific aspect even for a long-term mixing feature in spite of the difficulty in the quantitative comparison using its fractal dimension. The residence time distribution was also a potential analysis providing the flow structure with the time-information, and such analyses via various approaches enable the general evaluation of the mixing performance.

References

[1] J.M. Ottino, Mixing, chaotic advection, and turbulence, Ann. Rev. Fluid Mech. 22 (1990) 207–253.
[2] S. Murata, Y. Miyake, T. Inaba, Laminar flow in a helically coiled pipe, Bull. Jpn. Soc. Mech. Eng. 24 (188) (1981) 355–362.
[3] S.W. Jones, O.M. Thomas, H. Aref, Chaotic advection by laminar flow in a twisted pipe, J. Fluid Mech. 209 (1989) 335–357.
[4] N. Acharya, M. Sen, H. Chang, Heat transfer enhancement in coiled tubes by chaotic mixing, Int. J. Heat Mass Transfer 35 (10) (1992) 2475–2489.
[5] N. Acharya, M. Sen, H. Chang, Analysis of heat transfer enhancement in coiled-tube heat exchangers, Int. J. Heat Mass Transfer 44 (2001) 3189–3199.
[6] A. Mokrani, C. Castelain, H. Peerhossaini, The effects of chaotic advection on heat transfer, Int. J. Heat Mass Transfer 40 (13) (1997) 3089–3104.
[7] C. Castelain, A. Mokrani, P. Legentilhomme, H. Peerhossaini, Residence time distribution in twisted pipe flows: helically coiled system and chaotic system, Exp. Fluids 22 (1997) 359–368.
[8] C. Castelain, D. Berger, P. Legentilhomme, A. Mokrani, H. Peerhossaini, Experimental and numerical characterisation of mixing in a steady spatially chaotic flow by means of residence time distribution measurements, Int. J. Heat Mass Transfer 43 (2000) 3687–3700.
[9] C. Chagny, C. Castelain, H. Peerhossaini, Chaotic heat transfer for heat exchanger design and comparison with a regular regime for a large range of Reynolds numbers, Appl. Therm. Eng. 20 (2000) 1615–1648.
[10] T. Nakayama, T. Inaba, K. Satioh, Numerical investigation of laminar flow and heat transfer in multiple pipe bends, Trans. Jpn. Soc. Mech. Eng. 69 (688) (2003) 2664–2669.
[11] S.V. Patankar, D.B. Spalding, A calculation procedure for heat, mass and momentum transfer in three-dimensional parabolic flows, Int. J. Heat Mass Transfer 15 (1972) 1787–1806.
[12] K. Ghia, J.S. Sokhey, Laminar incompressible viscous flow in curved ducts of regular cross-sections, J. Fluids Eng. 99 (1977) 640–648.
[13] F.C. Moon, Chaotic and Fractal Dynamics, Wiley, New York, 1992, pp. 315–319.
[14] T. Atobe, M. Funakoshi, S. Inoue, Orbital instability and chaos in the Stokes flow between two eccentric cylinders, Fluid Dyn. Res. 16 (1995) 115–129.
[15] F.C. Moon, Chaotic and Fractal Dynamics, Wiley, New York, 1992, pp. 350–363.